Material mixing in shock-induced pseudotachylites, Vredefort impact structure, South Africa

Elizaveta Kovaleva[a*], Matthew S. Huber[a], Roger Dixon[b]

[a]*Department of Geology, University of the Free State, 205 Nelson Mandela Drive, 9300 Bloemfontein, South Africa*

[b]*Department of Geology, University of Pretoria, 0028 Pretoria, South Africa*

[*]*Corresponding author. E-mail address: kovalevae@ufs.ac.za*

***Highlights**

- Dolerite-hosted pseudotachylites contain exotic clasts of granite
- Within granite clasts, shocked zircon and monazite are in contact with one another
- Intermediate composition of pseudotachylites due to material mixing
- Material mobilized due to fracture dilation in dolerite
- Quartz phase transition allowed material mixing to take place
- Impact pseudotachylites are not strictly *in situ* melts

Graphical Abstract

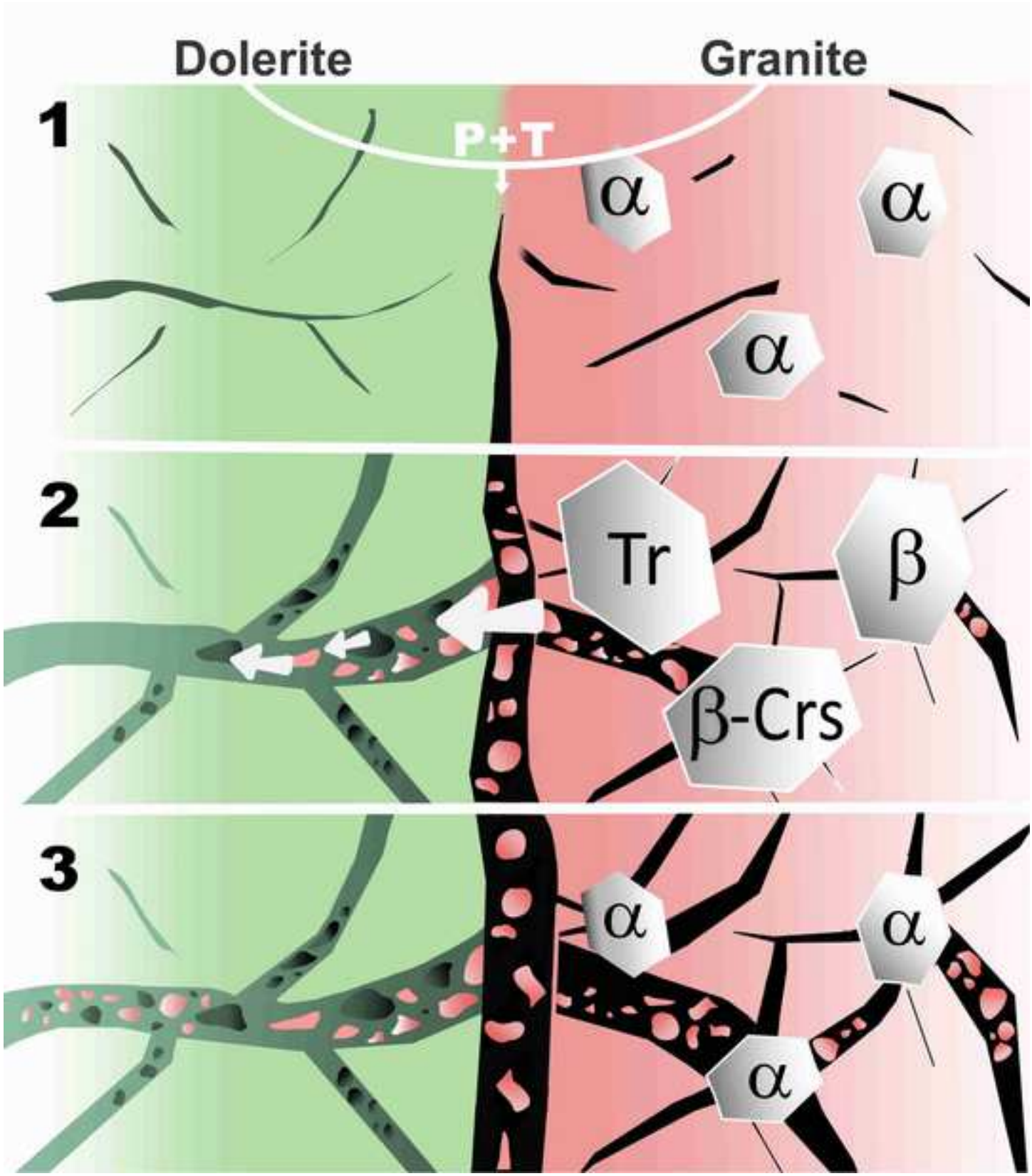

ABSTRACT

Impact-generated pseudotachylites (PTs) have been extensively studied in the Vredefort Impact Structure, South Africa, and have been shown to correspond chemically and isotopically to their host rocks. Such melts are frequently described as forming strictly *in situ* with lithic clasts derived from the immediate wall rocks. Mixed compositions are rare, where PTs are observed directly along a lithological contact. In this study, we document the presence of vast numbers of granitic clasts within dolerite-hosted PT veins within the Vredefort impact structure. The groundmasses of dolerite-hosted PT veins have two distinct geochemical compositions: (1) mafic, and (2) intermediate. The two compositional melt phases have a sharp contact, indicating immiscibility and/or mingling. Shocked zircon and monazite within the granite clasts enclosed in a dolerite-hosted PT vein indicate shock deformation prior to clast transport into the dolerite. In monazite, we report a new shock microtwin geometry 180°/[104].

The mechanisms by which granitic clasts were emplaced in the dolerite-hosted veins are complex. Previous experimental work has suggested that varying shock velocity in different lithologies may be responsible for material mixing. In addition, the thermal pulse accompanying the shock wave would have caused quartz in the granite to transform into volumetrically larger high-temperature polymorphs, significantly increasing the granite volume compared to the adjacent dolerite. Together with fluctuation of stresses (post-impact reverberations) after the passage of the main shock wave, this volume adjustment initiated brittle fracturing of the dolerite. A negative pressure gradient was thus generated within the dolerite that allowed granitic material to be injected into the dolerite-hosted melt veins.

1. Introduction

Impact generated pseudotachylites (PTs) are fine-crystalline melt veins and networks of veins (network breccia) from a few millimetres to tens of metres thick, laden with fragments of wall rock (Killick and Reimold, 1990; Reimold and Colliston, 1994). The exact mechanisms of formation are debated and may include shock melting, pore/cavity collapse at the shock wave front, decompression melting, friction melting, acoustic fluidization, shock recovery melting and post-impact seismic "shaking" (Garde and Klausen, 2016; Kowitz et al., 2013; Martini, 1978, 1991; Melosh, 2005; Reimold, 1995; Reimold et al., 2016; Spray, 2010). Pseudotachylites are abundant in the Vredefort impact structure core and have been observed in all pre-impact lithologies (Bisschoff, 1988).

The majority of studies in Vredefort have focused at the abundant and easily accessible PTs in granitic rocks in the Vredefort basement granite, in quarries and river pavements (Bisschoff, 1988; Harris et al., 2013; Lieger et al., 2011; Mohr-Westheide and Reimold, 2010; Mohr-Westheide et al., 2009; Reimold and Colliston, 1994; Reimold et al., 2016, 2017; Riller et al., 2010). Only a few studies at Vredefort have reported PT veins in mafic rocks, such as garnet hornfels (Bisschoff, 1988; Wilshire, 1971) and dolerite/gabbroic dikes and sills (Hart et al., 1999; Killick and Reimold, 1990). The mafic intrusions in the Greenlands Greenstone Complex show rare <1 cm-wide PT veinlets, but some contain up to 1 m-wide PT breccia zones, particularly occurring near lithological contacts with quartzite or shale (Reimold and Colliston, 1994).

Studies of PTs within Vredefort have consistently shown that their composition closely matches the composition of their host (Harris et al., 2013; Mohr-Westheide and Reimold, 2010; Reimold and Colliston, 1994; Reimold et al., 2016, 2017). Geochemically, PTs in felsic host rocks (granites, quartzites, shales) typically are slightly more mafic than their host rocks (Willemse, 1937; Wilshire, 1971), because of initial preferential ultracataclasis and

subsequent melting of ferromagnesian and hydrous minerals under non-equilibrium conditions. Preferential melting of certain phases occurs due to their low fracture toughness and low melting point (e.g., Spray, 2010). In contrast, PTs in mafic host rocks such as epidiorite, mafic lavas, garnet hornfels, or nepheline syenite, are more felsic than their host rock (Killick et al., 1988; Wilshire, 1971). This contradicts both the phenomenon of preferential fusion of mafic phases into PT melt and the idea of *in situ* formation (Maddock, 1992; Reimold and Colliston, 1994; Spray, 2010; Thompson and Spray, 1996). On the other hand, PTs hosted by more than one lithology, such as along lithological contacts, have mixed compositions, which include tectonic (Killick et al., 1988; Maddock, 1992), Sudbury (Thompson and Spray, 1996) and Vredefort PTs (Lieger et al., 2011; Reimold et al., 2017).

Typically, lithic clasts in PTs are derived from the immediate host rock (Mohr-Westheide and Reimold, 2010). A few authors have described singular exotic clasts (Reimold et al., 2016; Wilshire, 1971), and transport of clasts (Bisschoff, 1988), but no constraints or analyses of the transportation mechanism have been made. In this study, we examine PTs hosted entirely by mafic rocks, but containing a significant felsic component, including lithic clasts. We suggest a potential mechanism responsible for the observed compositional mixing and clast transport.

2. Geological Background

The Vredefort impact structure is located ~120 km SSW from Johannesburg, South Africa (Fig. 1A). The age of shock deformation is estimated at ~2020 ± 3 Ma (Kamo et al., 1996; Moser, 1997; Spray et al., 1995). Only the central uplift of the structure is preserved, as the structure was deeply eroded to the depth of ~8–10 km after the impact event (Schreyer, 1983). The visible diameter of the central uplift is 100–120 km along its N-S axis (Bisschoff, 1988). Geophysical modelling (Henkel and Reimold, 1998) suggested that the original impact

structure was ~250 km in diameter, whereas numerical modelling (Ivanov, 2005) suggested an initial diameter of ~180 km. The Vredefort structure is also notable for the presence of shallow Moho beneath the structure (Youssof et al., 2013).

The Outer Granite Gneiss (OGG) tonalite-trondhjemite-granodiorite (TTG) suite is exposed at the surface within the core of the structure (Fig. 1A). The OGG has a whole-rock ^{87}Rb, ^{232}Th, ^{238}U and ^{235}U isotopic ages of 3.05 Ga and experienced regional metamorphism at 2.8 Ga (Hart et al., 1981). U-Pb dating of zircon from the OGG suite by Kamo et al. (1996) yielded an average of 3.03 Ga, roughly consistent with the whole rock dating by Hart et al. (1981). The basement granites are intruded by abundant dolerite dikes and small bodies that are shocked, but not tectonically deformed, and have a U-Pb zircon age of $\geq$ 2560 Ma, suggesting Ventersdorp age of intrusions (Hart et al., 1999). These dolerite intrusions are often cut by impact-generated PT veins (Hart et al., 1999; Killick and Reimold, 1990).

3. Field Observations

Samples for this study were collected from the granitic core of the structure (Fig. 1A). Metamorphosed basement granite in contact with a dolerite intrusion is exposed southwest of Parys near the Lesothospruit creek (26°57'09.2"S 27°22'51.4"E). The granite is pink, coarse-grained, deformed, foliated, has typical granitic mineralogy (biotite, quartz, and feldspars), and locally contains migmatites. Apatite, zircon, and monazite are accessory phases. The dolerite is exposed in a 100 x 80 m (8 000 m^2) outcrop surrounded by granite. In the contour map of the magnetic data (reduced to the pole), recorded across the study area, dolerite extends below the erosional level as an oval body of ca. 100 x 60 m, stretching from WSW to ENE (Kovaleva et al., 2018). The dolerite has a massive and uniform texture with no evidence of foliation and is grey on fresh surfaces and brown on weathered surfaces. It is composed of medium-grained (up to 2 mm) laths of plagioclase (up to 70 vol. %), grains of

clinopyroxene, amphibole, ilmenite, and rare crystals of olivine (for additional field descriptions and magnetometer survey results see Kovaleva et al., 2018).

Pseudotachylites crosscut both the granite and dolerite. The abundance and thickness of PTs in both rocks decrease with increasing distance from their lithological contact. The PT veins in granite are dark-grey to black and contain numerous clasts of the wall rock, but exotic clasts (e.g., dolerite) have not been observed, even though PT veins up to 20 cm thick are abundant in granite. Within the dolerite, PT veins occur up to 12 cm thick; they are dark-grey or brown and contain numerous angular to rounded clasts of both dolerite and granite, with clast size ranging from a few mm to a few cm. The PT veins in dolerite are not uniform, with some veins having clasts of only dolerite (herein described as Melt 1) and some veins having clasts of both dolerite and granite (herein described as Melt 2, Fig. 1B-C). Granite clasts within the dolerite-hosted PT veins are up to 7 cm in diameter, decreasing in size and abundance with increasing distance from the contact with granite towards the centre of the dolerite outcrop. Veins containing granite clasts strike at 179° and 305° into the dolerite body, i.e., the granite clasts are introduced from different directions with respect to the crater centre. We observed hundreds to thousands of granitic clasts within dolerite-hosted PT veins over an area of approximately 30 m^2 and intruding up to 13 m from the contact.

The contact between granite and dolerite is not directly exposed, but can be inferred. Between dolerite and granite outcrops, along the inferred contact, a wide zone (varying from 30 cm to 4 m in width) of massive PT is exposed (Fig. 1D), which surrounds the dolerite intrusion on all sides. This rock is dark-grey, has a fine-crystalline matrix, and contains multiple granitic clasts (locally up to 70%) of various sizes and shapes, but no dolerite clasts are observed (Fig. 1D).

4. Samples and Methods

4.1. Optical and scanning electron microscopy (SEM)

We collected representative samples of granite and dolerite with PT veins, as well as massive PTs along the granite-dolerite contact, and dolerite samples with PT veins that do not have visible granite clasts ("Melt 1") and PT veins that have granite clasts ("Melt 2"). Polished petrographic thin sections were prepared for samples of dolerite, contact zone, and granite, and were analysed with an Olympus BX51 optical microscope equipped with an Olympus U-TVO.63XC camera (Department of Geology, University of the Free State). Thin sections were studied using a Jeol JSM-6610 SEM equipped with an energy-dispersive Thermo Scientific Ultradry X-ray (EDX) spectrometer (Department of Geology, University of the Free State). The EDX detector was used to identify mineral phases qualitatively. The analytical conditions for collecting the backscattered electron (BSE) images and qualitative chemical maps were 15 KV accelerating voltage, 8 nA probe current, 10 mm working distance, and a 9.6 x 10^{-5} Pa vacuum.

4.2. Wavelength dispersive X-ray fluorescence (WD-XRF)

Samples were analysed at the Department of Geology, University of the Free State. Samples were crushed to powder for fusion discs (used for elements of major quantities) and pressed pellets (used to measure Na and trace element contents). For the fusion discs, 10 g of powder was heated to 110°C to dehydrate and devolatilize the sample, which was then heated to 1050°C to break down minerals such as carbonates and produce the indicated total loss on ignition (LOI). 0.28 g of the sample was mixed with flux (0.2445 g La_2O_3, 0.705 g $Li_2B_4O_7$, 0.5505 g Li_2CO_3, and 0.02 g $NaNO_3$), melted at 1000°C for approximately 5 min in a Pt crucible and cast into a disc. The pressed pellet was prepared by adding 8 g of the sample to 3 g of Hoechst wax ($C_6H_8O_3N_2$), mixing for 20 min in a Turbula mixer to ensure homogeneity and pressed at > 395 N/m^2.

Chemical analyses were conducted using a PANalytical Axios WD-XRF machine, with an Rh end window tube, 4 kW Rh anode, and a W cathode filament (Department of Geology, University of the Free State). The applications included "IGS majors", "UIC traces" and "Sodium only." Zn, Zr, P, Cd, and Ag were measured for correction of line overlaps. Raw data were processed with X-ray analyses software SuperQ 4.0R with the toolbox for trace elements Pro-Trace (PANalytical B.V.).

4.3. Energy-dispersive micro-X-ray fluorescence spectrometry (μ-ED-XRF)

The interior of a sample of dolerite was mapped for element distribution using a Bruker M4 Tornado μ-ED-XRF spectrometer at the Stoneman Laboratory, University of Pretoria. The instrument has a large analytical area, up to 20 x 16 cm, and can hold a mass of up to 5 kg, so samples for were cut and ground flat with no further sample preparation. Elemental imaging is characterized with a complete element spectrum for each pixel, and the processed image can be assembled from the addition of user-selected element spectra.

The instrument was configured with a Rhodium tube operated at 50 kV, 500 μA and 30 W. The polychromatic beam (0–50 keV) was focused by means of a polycapillary lens to a spot size of < 25 μm at this wavelength, with the incident beam and take-off angles at 51°. The instrument is equipped with two silicon drift detectors with an energy resolution of 145 eV for Mn Kα, which face each other at a 180° angle and 90° to the tube with respect to the sample surface. The sample chamber was evacuated to < 20 mbar to enable light elements such as sodium to be measured. Typically, step size and integration time per pixel were set to 100 μm and 50 ms. Selected smaller areas were scanned at a step size of 50 μm, for greater resolution.

4.4. Electron backscatter diffraction (EBSD) analysis

Crystallographic orientation mapping of deformed zircon and monazite grains by EBSD was performed at the Laboratory for scanning electron microscopy and focused ion beam applications at the University of Vienna, Austria.

The thin section sample was chemo-mechanically polished using Struers OP-S Suspension of colloidal silica, and a rotary-head polishing machine. The polished sample was carbon-coated with a thin carbon layer (5-10 nm). Orientation contrast images were produced using an FSE detector mounted on the EBSD-tube of an FEI Quanta 3D FEG instrument, equipped with a Schottky field emission electron source, an EDAX Pegasus Apex 4 system consisting of a Digiview IV EBSD camera and an Apollo XV silicon drift detector for EDX analysis. Electron beam conditions for analyses were 15 kV accelerating voltage, 4 nA probe current using the analytic mode. Stage settings were at 70° tilt and 14 mm working distance. After potentially deformed crystals were identified based on orientation contrast images, EBSD crystallographic orientation mapping was applied to selected zircon and monazite crystals. An EBSD camera binning of 4 x 4 was used to index single frame data at 49 ms exposure time, reaching indexing rates of ca. 20 points per second. The Kikuchi pattern contrast was improved by applying both static and dynamic background subtraction and intensity histogram normalization. Hough transformation settings were at 120 x 120 pixels binned pattern size and 1° Theta step size, while the Rho fraction was limited to the inner 88% of the Kikuchi pattern. A 9 x 9 convolution mask was applied to index 3 – 15 peaks with a minimum peak distance of 8 pixels in Hough space. The following lattice parameters were used for reference: Zircon, di-tetragonal, Laue group 4/mmm, a=b=6.612 Å, c=5.983 Å, α=β=γ=90° (Finch et al., 2001); Monazite: monoclinic prismatic, Laue group 2/m, a=6.79 Å, b=7.02 Å, c=6.467 Å, α=γ=90°, β=103.38° (Ni et al., 1995). Map data were collected in hexagonal grid mode using step sizes of 220 nm for the zircon map, and 120 nm for the monazite map. The EDX intensities and EBSD data were collected simultaneously using

OIM v7.3 data collection software. The EBSD data were re-indexed, plotted and analysed with EDAX OIM v7.3 analysis software. Data re-indexing was assisted by assigning data points to phases based on selected EDX intensity ranges in EDX energy regions of interest. Crystal orientation maps were cleaned using the Confidence Index Standardization (CIS) procedure, which unifies the confidence index of equally oriented points within a grain (presuming a minimum grain size of 3 pixels in more than one row, and a tolerance angle of 5°). The Confidence Index (CI) represents the difference in the number of triangles (found between three bands each) between the first and second orientation solution, divided by the total number of identified triangles. No orientation data were changed during clean-up. The data were filtered for CI > 0.05 for the zircon map and CI > 0.1 for the monazite map to exclude single, statistically poor data points, which do not belong to a "grain."

5. Results

5.1. XRF data: composition of target rocks and associated PT veins

Chemical analyses of two samples of dolerite, one sample of PT in dolerite without granite clasts (Melt 1), one sample of PT in dolerite with granitic clasts (Melt 2), three samples of massive PT from the contact zone, two samples of granite and two samples of PT in the granite are summarized in Tables 1 and 2.

Melt 1 is geochemically close to the host dolerite, having a more mafic picro-basaltic composition (Fig. 2A). This is consistent with the fracture toughness and breakdown temperature values for various minerals, with the lowest values for micas, inosilicates being in the middle, and feldspars being the toughest and the most refractory (Spray, 2010). Therefore, it is expected that the PT melt in dolerite is depleted in Na and K compared host dolerite (Fig. 2A), as the feldspars in dolerite should be breaking down and melting last. The composition of Melt 2 is andesitic (Fig. 2A). It is intermediate between the compositional

range of granite and dolerite for both major and trace elements, suggesting approximately equal mixing of granite and dolerite (Fig. 2A, B). For trace elements, the elemental proportions are variable, possibly suggesting incomplete mixing or nugget effects. The PT extracted from granite and massive PT from the contact zone are geochemically indistinguishable from the analysed granite, with only a slight shift towards more mafic compositions. The compositional shift is also consistent with preferential melting of mafic phases prior to felsic phases, as has been documented in previous works (e.g., Wilshire, 1971).

5.2. Sample surface description and compositional mapping

A representative sample of dolerite (~10 x 14 cm) with PT veins containing both Melt 1 and Melt 2 was chemically mapped. In this sample, Melt 2 is optically slightly darker in colour than Melt 1 (Fig. 3A-B). The largest granitic clast within Melt 2 is ~1 x 2 cm in size, irregularly-shaped, rounded at the edges, and is composed primarily of quartz and feldspar, with some biotite and accessory apatite. Numerous smaller (< 2 mm) fragments of quartz and feldspar are present within Melt 2. Coarse-grained areas of the dolerite in the centre of the sample are surrounded by PT veins and either represent a variation of grain size in host dolerite, or exotic gabbroic clasts (Fig. 3D). For further details about the microstructures of the Melt 1 PTs in the dolerite, see Kovaleva et al. (2018).

Compositional mapping by µXRF confirms the existence of two distinct compositional domains of PT (Fig. 3C-D). Melt 1 is homogeneous in composition. Coarse-grained dolerite clasts are found within Melt 1. Melt 2 contains conspicuous fine-grained and coarse-grained inclusions of dolerite (Fig. 3C-D). Si-rich clasts in Melt 2 are compositionally distinct from the host rock (Fig. 3C-D) and are absent in Melt 1.

Between Melt 1 and Melt 2, a sharp boundary is defined by a compositional shift in Ba, Ca, Co, Fe, K, Mn, Si, and Sr, which is likely a result of the immiscible mingling of the two melts (Fig. 3C, lower left to top centre). An enrichment of K, Sr, and Si in Melt 2 (Fig. 3D) is consistent with disaggregated and melted quartz and K-feldspar from granite. A depletion in Fe and Ca in Melt 2 points to a dilution of a mafic component. A lens of Melt 2 ~1 cm long is completely enclosed in Melt 1 within the surface of the sample (Fig. 3A, arrow).

5.3. SEM and EBSD data: Shocked minerals

In thin section, an elongated fractured granitic clast ~8 x 3 mm within a Melt 2 vein (Fig. 4A) consists of plagioclase, quartz, K-feldspar, and biotite. Zircon, monazite, apatite, and FeO are accessory phases (Fig. 4B). The clast contains adjacent grains of shocked zircon and monazite (Fig. 5).

The euhedral zircon grain is 70 x 45 µm and is fractured in the central part with small displacements. Zircon preserves initial growth zoning (non-indexed zones in Fig. 5A) and hosts a number of (sub)grains that are up to 5 µm in diameter and have a cumulative misorientation of > 15°. These (sub)grains are isometric to elongate and are concentrated along fractures or at fracture intersects. Besides, zircon grain contains one discontinuous microtwin lamella, 300–500 nm thick, and is 25 µm long in its longest section. The lamella is crystallographically rotated by 65° with respect to the host crystal, sharing one of the <110> axes with the host (Fig. 5B).

The monazite is adjacent to the zircon grain, has a sub-angular shape, and is 20 x 15 µm in size. The monazite displays moderate crystal-plastic deformation (> 15° intragranular misorientation) with a checkerboard lattice distortion pattern and hosts two sets of short (< 5 µm), up to 1 µm thick, irregularly-spaced microtwin lamellae (Fig. 5C). Both twin sets in monazite are rotated crystallographically by 180° with respect to the host, sharing the [010]

axis with the host crystal, while twin lamellae set 1 also shares the [001] axis (Fig. 5D). Axes [100] of both sets are symmetrically rotated about [100] of the main grain by ~25°. Grain boundary analyses show that twin set 1 is rotated about the [100] crystallographic axis, whereas set 2 is rotated about the [104] crystallographic axis of the host crystal, thus giving the twin relationships 180°/[100] and 180°/[104] respectively.

6. Discussion

6.1. Nature of the dolerite-hosted veins

The dolerite-hosted veins have qualities consistent with forming as a melt rather than as a cataclasite. Some researchers have stated that the original nature of the veins in Vredefort cannot be distinguished due to recrystallization and overprinting of veins (e.g., Reimold, 1995; Reimold and Gibson, 2005). Although this lack of distinctiveness holds true in many examples, in the case of the dolerite-hosted PT veins examined in this study, several lines of evidence point to the presence of melt rather than cataclasite. Firstly, the inclusion of relatively large granitic clasts compared to the thickness of the veins up to distances of 13 m from the visible dolerite-granite contact shows that the conditions allowed for the flow of material without mechanical disaggregation as might be expected in a cataclasite. Secondly, the mingling structures at the compositional boundary between Melt 1 and Melt 2 (Fig. 3) suggest the existence of two immiscible fluids in contact with one another. Thirdly, the intermediate chemical composition of Melt 2 between basaltic and dacitic (Fig. 2) suggests efficient compositional mixing of granite and dolerite, which is most likely achieved by a melt. Additional textural relationships are described by Kovaleva et al. (2018).

6.2. Exotic clasts in pseudotachylite

In this study, we observed an unusual relationship between PT and host rocks that appears to contradict traditional thinking on PT formation in Vredefort (Reimold et al., 2016; 2017). In natural samples, PT vein compositions have repeatedly been shown to correspond to the host rock (Harris et al., 2013; Reimold et al., 2016, 2017), and have been suggested to form exclusively *in situ* without any significant material transport (Mohr-Westheide and Reimold, 2010; Reimold et al., 2017). At least one study, however, expressed the opposite opinion that pseudotachylite could represent allochtonous melt (Lieger et al., 2011).

Our data demonstrate that abundant exotic clasts can be transported within PT melt veins for distances of at least tens of metres. This is unlike similar occurrences reported in the Vredefort structure, where compositionally mixed PTs develop along a contact between contrasting lithologies, e.g., granite and amphibolite in contact at the Kudu quarry (Reimold et al., 2016). In that case, the PT is parallel to the lithological contact and contains clasts derived from both walls. Notably, the massive PT developed along the contact in the present study does not show mixed composition, but is granitic (Fig. 2, Table 1). In another Vredefort location (the Otavi quarry), PT is hosted by granite gneisses and contains a few large rounded clasts of dolerite (Reimold et al., 2016). There, the PT veins are several metres thick, and thus the inclusion of dolerite clasts is likely caused by the total disaggregation of a small dolerite dyke or sill and its incorporation into a larger melt dyke, rather than transmission of clasts through a narrow PT vein. Field examinations of the area around the Otavi quarry by us and previous researchers (Reimold et al., 2016), have not revealed the location of the dolerite parent body, suggesting that it was completely disaggregated and incorporated within a massive PT dyke with a predominantly granitic composition.

6.3. Nature vs. experiment

Kenkmann et al. (2000) experimentally shocked a composite sample of dunite and quartzite, thereby generating melt along the contact. In the experimental product, the melt intruded into one of the two adjacent lithologies and terminated as clast-bearing injection veins. This provides a similar case to the observations of dolerite in contact with granite described in our study. The different response to the pressure waves propagation by granite and dolerite created a thick zone of clast-laden melt between the two.

However, the findings of Kenkmann et al. (2000) show that the injection veins more frequently intrude into quartzite, because the higher shock velocity within dunite enhanced material transport from mafic to felsic rock, but not in the opposite direction (Heider and Kenkmann, 2003). These observations contrast with the Vredefort outcrops reported in this study, where firstly, PTs were developed on both sides of the lithological contact and secondly, felsic material was transported into mafic rock, and not *vice versa*. In the sampled outcrop, thousands of granitic clasts were transported sufficiently far into a dolerite-hosted PT to allow their incorporation into dolerite melt (Figs. 2, 3). The substantial difference between experimental and field observations show that either the lithological differences between nature and experiment (granite-dolerite vs. quartzite-dunite interface, respectively) substantially changes the nature of the interaction, or that not all natural factors could be accounted for in a small-scale experiment. Importantly, the experimental work of Kenkmann et al. (2000) was performed on rocks that were not under lithostatic pressure, as opposed to the deeply buried rocks at Vredefort. Both rock types in the experiment thus would have been in the brittle deformation regime, whereas in the case presented here, the granite was in a ductile deformation regime, while the adjacent dolerite was close to the brittle regime (Kovaleva et al., 2018).

Moreover, the duration of experiment was only several seconds before the sample was quenched, which did not allow for further development of PT that occurs in the impact

process, where the rocks continue experiencing post-shock deformation effects after the impact (i.e., central uplift collapse, crater modification, post-impact thermal overprint, etc.). Discrepancies between natural observations and experimental products may also suggest that a previously undocumented and/or unconsidered mechanism(s) affected PTs development during the Vredefort impact event. The missing mechanism(s) can be constrained based on the field relationships, the timing of deformation, and the composition of the rocks involved.

6.4. Field constraints

The geometry of the system was constrained based on field relationships. The pseudotachylite that rings the dolerite outcrop has a large exposure. In total, an area of ca. 8 000 m^2 of dolerite outcrops, enclosed into pseudotachylite with granitic composition, was investigated in the field. The zone of massive PT developed at the lithological contact contains disaggregated clasts of granite, but not dolerite. There is no evidence of dolerite migrating into granite in the field observations, hand sample observations, or in the geochemical analyses (Fig. 2). This melt zone could be analogous to the early PTs produced in experiments of Kenkmann et al. (2000) and is a reasonable source of granite clasts injected into dolerite-hosted PT veins.

The thickness and frequency of PT veins in dolerite are greatest near the contact and have the highest abundance of exotic granite clasts. Dolerite outcrops > 12–13 m from the contact with granite have either no PT veins or thin (< 1 cm thick) veins filled with Melt 1 with no exotic clasts. Although we cannot constrain the vertical component (i.e., the amount of dolerite that has eroded away), based on observations of the two dimensional relationships and geophysical data (Kovaleva et al., 2018), the dolerite was most likely extending vertically either as a diapir or as a sill. In either case, the distances to the contact in a vertical direction would not appear to be significantly less than the observed distance to the exposed contact.

Importantly, the direction of movement of granite clasts into dolerite body was inconsistent in every outcrop examined, where granite clasts were trapped in veins with varying orientations.

6.5. Timing constraints based on shock microstructures

The timing of events is constrained by the presence of shocked minerals within granite clasts. Zircon {112} shock microtwins are thin lamellae that are rotated by 65° about the [110] axis of the host zircon (Cavosie et al., 2015; Moser et al., 2011), consistent with the lamellae observed in this study. Shocked monazite has at least 12 distinct documented orientations of shock microtwins (Erickson et al., 2016, 2017), of which, the 180º/[100] relationship is present in shock twin set 1. The geometry of shock twin set 2 (180°/[104]) has not been described previously, thus representing a new shock twin relationship.

This shock deformation must have occurred prior to fragmentation and granite clast incorporation into the dolerite. Extreme differential stress, required to form shock microtwins in zircon (Jones et al., 2018), most likely corresponds to the interaction of the rarefaction wave with the shock wave (Cox et al., 2018; Huber and Kovaleva, 2019). Because the host PT vein could not have formed before the passage of the shock wave, the granite must have been shocked before its fragments were incorporated into the PT vein. Therefore, the presence of shocked monazite and zircon strongly suggests that these events took place in the following order: 1) shock deformation of zircon and monazite; 2) disaggregation of the host granite, liberating the clast hosting shocked minerals; 3) transport and inclusion of the granite clasts into dolerite-hosted PT veins.

6.6. Material mixing model

6.6.1. Difference in deformation regimes

To drive material from one lithology towards another at depth, a driving force must be present, and that force must have been related to the conditions of the two lithologies during and immediately after the shock event. A schematic diagram showing the material migration process is presented in the Figure 9.

The granite and dolerite were most likely located at depths of 10–15 km before the impact, where the granite was close to the brittle-ductile transition, and the dolerite was in the brittle regime (Kovaleva et al., 2018). Fluctuating stresses during the post-shock reverberations following the passage of the primary shock wave initiated brittle fracturing in dolerite, cataclasis and melting followed by incipient opening of the fractures (see below).

6.6.2. Role of quartz in fracturing

A key compositional difference in the sampled outcrops is the presence of quartz in the granite and absence in the dolerite. Post-shock elevated temperatures (Kenkmann et al., 2000; Potter et al., 2013) must transform silica to high-temperature polymorphs (Fig. 6; e.g., Hartlieb et al., 2016), including β-quartz (573ºC at atmospheric pressure), tridymite (870ºC at atmospheric pressure), and β-cristobalite (900ºC at atmospheric pressure; Ohno et al., 2006; temperatures of phase transitions at varying pressure can be read from Fig. 6). The molar volume of α-quartz is 22.688 cm^3/mol, and β-quartz is 23.865 cm^3/mol (Swamy and Saxena, 1994; Fig. 7). Tridymite can exist in multiple crystal systems, ranging in volume from 26.530 cm^3/mol to 27.510 cm^3/mol (Swamy and Saxena, 1994). Alpha-cristobalite is 25.739 cm^3/mol, and β-cristobalite is 27.40 cm^3/mol (Swamy and Saxena, 1994). In experiments, these phase transitions occur instantaneously with the onset of elevated temperatures and cumulatively result in as much as 37 vol. % thermal expansion of SiO_2 (Ringdalen, 2014), and substantially more thermal expansion of granite directly compared to basalt (Hartlieb et

al., 2016). Basement granitoids within the Vredefort structure have up to 50% quartz content, which would potentially result in volume expansion in granite up to 18.5%.

At pressures up to 2-4 GPa, the transition temperatures vary insignificantly, increasing with increasing pressure; and above the 2-4 GPa pressure range, all silica phases transform to coesite (Fig. 6). Evidence of the SiO_2 phase transition to cristobalite and tridymite are known in many younger impact structures and should occur in all shock metamorphic settings (e.g., Ferrière et al., 2009). Unfortunately, at Vredefort, there is poor preservation of SiO_2 phase transitions due to the well-documented post-impact thermal overprint (e.g., Gibson et al., 1998, 2002; Kamo et al., 1996; Martini, 1978; 1991; Reimold et al., 2002). Grossly recrystallized and partially molten quartz clasts from the PT in granite are shown in optical images in Figure 8; similar textures are presented in Reimold et al. (2016) from a different Vredefort locality.

The volumetrically larger high-temperature phases induced a volume imbalance in the crust, as the expanded granite needed to be spatially accommodated. As the granite was under high confining pressure, the only direction of accommodation would be vertical. Meanwhile, the dolerite body that was entirely enclosed within the granite did not experience internal volume expansion. Dolerite was dragged and deformed by the expanding host granite, with extension accommodated by brittle fractures. The dilation of fractures would cause a negative pressure gradient that would allow for material (clasts and melt) migration from the surrounding granitic pseudotachylite envelope (Fig. 9).

In impact conditions, granitic melt can obtain low enough viscosity to migrate rapidly (Melosh, 2005). Thus, the andesitic composition of some of the veins in dolerite could have been achieved not only by migration and partial incorporation of granite clasts, but also by mixing with granitic melt, which was possible at initial impact-generated temperatures, and consistent with our observations (Fig. 3). When the system cooled and collapsed, the

fractures closed, which allowed for the clasts that are larger in diameter than their host veins to be present in the dolerite (Fig. 4a).

These mechanisms predict that material transport between lithologies is more likely to occur from a felsic rock to a mafic rock and may also explain the observations of a more felsic PT composition in some mafic hosts (e.g., Wilshire, 1971), and granite clast transport into dolerite-hosted PT veins.

7. Conclusions and Implications

Presently, 200 impact structures are known on Earth (Schmieder and Kring, 2020). Practically all of the impact structures formed in targets of mixed lithology. Experimental and numerical studies on impact events often focus on the effects of shock deformation using a simplified, essentially homogeneous target composition. Our work shows that mixing of material can occur during the cratering process, even at the deep stratigraphic levels. This interaction of lithologies is not well understood.

This study demonstrates that PTs might not have the same composition as their host rocks, despite repeated studies from numerous groups demonstrating the compositional similarity between host rock and PT vein (therefrom “monomict breccia”). A possible reason for such discrepancy is that the majority of the studies in Vredefort have focused on granite-hosted PT veins. In order to study the effect of material transport in PT veins, it is necessary to find host lithologies that are not homogeneous. We suggest that literature describing the similarity of PTs and their host rocks may not always be applicable to large impact structures with inhomogeneous target rocks.

Acknowledgments

This work was supported by the National Research Foundation (NRF) [grant numbers 98443, 106511], received by E.K. We are grateful to C. van Rensburg and A.J. van Coller for the access to outcrops. We acknowledge J. Choane for preparing the samples and M. Purchase for obtaining the XRF data. L. Pittarello is acknowledged for her useful comments and discussions. Thanks to G. Habler for assisting in EBSD data collection and processing, and for her useful comments. W.U. Reimold and N. Timms are thanked for commenting on the earlier versions of this work. R. van der Westhuizen prepared an illustration for this study (Fig. 9). We are grateful to L. van der Westhuizen for the proof-reading of the final version of the manuscript. The editor M. Scambelluri is thanked for his editorial handling and reviewers A. Garde, P. Buchanan and J. Melosh are acknowledged for their useful comments and suggestions.

References

Bisschoff, A.A., 1988. The history and origin of the Vredefort Dome. Suid-Afrikaanse Tydskrif Vir Wetenskap 84, 413–417.

Buchanan, P.C., Reimold, W.U., 2002. Planar deformation features and impact glass in inclusions from the Vredefort Granophyre, South Africa. Meteoritics & Planetary Science 37, 807–822.

Cavosie, A.J., Erickson, T.M., Timms, N.E., Reddy, S.M., Talavera, C., Montalvo, S.D., Pincus, M.R., Gibbon, R.J., Moser, D., 2015. A terrestrial perspective on using ex situ shocked zircons to date lunar impacts. Geology 43, 999–1002.

Cox, M.A., Cavosie, A.J., Bland, P.A., Miljković, K., Wingate, M.T.D., 2018. Microstructural dynamics of central uplifts: Reidite offset by zircon twins at the Woodleigh impact structure, Australia. Geology 46, 983–986.

Erickson, T.M., Cavosie, A.J., Pearce, M.A., Timms, N.E., Reddy, S.M., 2016. Empirical constraints on shock features in monazite using shocked zircon inclusions. Geology 44, 635–638.

Erickson, T.M., Timms, N.E., Kirkland, C.L., Tohver, E., Cavosie, A.J., Pearce, M.A., Reddy, S.M., 2017. Shocked monazite chronometry: integrating microstructural and in situ isotopic age data for determining precise impact ages. Contributions to Mineralogy and Petrology 172, 11.

Ferrière, L., Koeberl, C., Reimold, W.U., 2009. Characterisation of ballen quartz and cristobalite in impact breccias: new observations and constraints on ballen formation. European Journal of Mineralogy 21, 203–217.

Finch, R.J, Hanchar, J.M., Hoskin, P.W.O., Burns, P.C., 2001. Rare-earth elements in synthetic zircon: Part 2. A single-crystal X-ray study of xenotime substitution. American Mineralogist 86, 681–689.

Fiske, P.S., Nellis, W.J., Lipp, M., Lorenzana, H., Kikuchi, M., Syono, Y., 1995. Pseudotachylites generated in shock experiments: Implications for impact cratering products and processes. Science 270, 281–283.

Gibson, R.L., Reimold, W.U., Stevens, G., 1998. Thermal-metamorphic signature of an impact event in the Vredefort Dome, South Africa. Geology 26, 787–790.

Gibson, R.L., Reimold, W.U., Ashley, A.J., Koeberl, C., 2002. Metamorphism on the Moon: A terrestrial analogue in the Vredefort dome, South Africa? Geology 30, 475–478.

Grieve, R.A.F., Langenhorst, F., Stöffler, D., 1996. Shock metamorphism of quartz in nature and experiment: II. Significance in geoscience. Meteoritics & Planetary Science 31, 6–35.

Harris, C., Fourie, D. S. and Fagereng, A., 2013. Stable isotope evidence for impact-related pseudotachylite formation at Vredefort by local melting of dry rocks. South African Journal of Geology 116, 101–118.

Hart, R.J., Welke, H.J., Nicolaysen, L.O., 1981. Geochronology of the deep profile through Archean basement at Vredefort, with implications for early crustal evolution. Journal of Geophysical Research 86, 10663–10680.

Hart, R.J., Moser. D., Andreoli, M., 1999. Archean age for the granulite facies metamorphism near the center of the Vredefort structure, South Africa. Geology 27, 1091–1094.

Hartlieb, P., Toifl, M., Kuchar, F., Meisels, R., Antretter, T., 2016. Thermo-physical properties of selected hard rocks and their relation to microwave-assisted comminution. Minerals Engineering 91, 34–41.

Heider, N., Kenkmann, T., 2003. Numerical simulation of temperature effects at fissures due to shock loading. Meteoritics & Planetary Science 38, 1451–1460.

Henkel, H., Reimold, W.U., 1998. Integrated geophysical modelling of a giant, complex impact structure: anatomy of the Vredefort Structure, South Africa. Tectonophysics 287, 1–20.

Huber, M.S., Kovaleva, E., 2019. Microstructural dynamics of central uplifts: reidite offset by zircon twins at the Woodleigh impact structure, Australia: COMMENT. Geology 47, e465.

Ivanov, B.A., 2005. Numerical modeling of the largest terrestrial meteorite craters. Solar System Research 39, 381–409.

Ivanov, B.A., Deutsch, A., 1999. Sudbury impact event: Cratering mechanics and thermal history, in: Dressler, B.O., Sharpton, V.L. (Eds.), Large meteorite impacts and planetary evolution II. Geological Society of America Special Paper 339, Boulder, Colorado, pp. 389–397.

Jones, G., Moser, D.E., Shieh, S.R., 2018. A numerical model for twin nucleation in shocked zircon and comparison with natural samples. Geophysical Research Letters 45, 10298–10304.

Kamo, S.L., Reimold, W.U., Krogh, T.E., Colliston, W.P., 1996. A 2.023 Ga age for the Vredefort impact event and a first report of shock metamorphosed zircons in pseudotachylitic breccias and Granophyre. Earth and Planetary Science Letters 144, 369–387.

Kenkmann, T., Hornemann, U., Stöffler, D., 2000. Experimental generation of shock-induced pseudotachylites. Meteoritics & Planetary Science 35, 1275–1290.

Killick, A.M., Reimold, W.U., 1990. Review of the pseudotachylites in and around the Vredefort "Dome", South Africa. South African Journal of Geology 93, 350–365.

Killick, A.M., Thwaites, A.M., Germs, G.J.B., Schoch, A.E., 1988. Pseudotachylite associated with a bedding-parallel fault zone between the Witwatersrand and Ventersdorp Supergroups, South Africa. Geologische Rundschau 77, 329–344.

Kovaleva, E., Huber, M.S., Fourie, F., Pittarello, L., 2018. Comparative study of pseudotachylite microstructures in mafic and felsic rocks from the Vredefort impact structure, South Africa. Implications for the experimental studies. South African Journal of Geology 121, 403–420.

Kowitz, A., Güldemeister, N., Reimold, W.U., Schmitt, R.T. and Wünnemann, K., 2013. Diaplectic quartz glass and SiO_2 melt experimentally generated at only 5 GPa shock pressure in porous sandstone: Laboratory observations and meso-scale numerical modeling. Earth and Planetary Science Letters 384, 17-26.

LeBas, M.J., LeMaitre, R.W., Streckeisen, A., Zenettin, B., 1986. A chemical classification of volcanic rocks based on the total alkali-silica diagram. Journal of Petrology 27, 745–750.

Lieger, D., Riller, U., Gibson, R.L., 2011. Petrographic and geochemical evidence for an allochthonous, possibly impact melt, origin of pseudotachylite from the Vredefort Dome, South Africa. Geochimica et Cosmochimica Acta 75, 4490–4514.

Maddock, R.H., 1992. Effect of lithology, cataclasis and melting on the composition of fault-generated pseudotachylites, Lewisian gneiss, Scotland. Tectonophysics 204, 261–278.

Martini, J.E.J., 1978. Coesite and stishovite in the Vredefort Dome, South Africa. Nature 272, 715–717.

Martini, J.E.J., 1991. The nature, distribution and genesis of the coesite and stishovite associated with the pseudotachylite of the Vredefort Dome, South Africa. Earth and Planetary Science Letters 103, 285–300.

Melosh, H.J., 2005. The mechanics of pseudotachylite formation in impact events, in: Koeberl, C., Henkel, H. (Eds.), Impact tectonics. Springer, Berlin Heidelberg, pp. 55–80.

Mohr-Westheide, T., Reimold, W.U., 2010. Microchemical investigation of small-scale pseudotachylitic breccias from the Archaean gneiss of the Vredefort Dome, South Africa, in: Gibson, L.R., Reimold, W.U. (Eds.), Large Meteorite Impacts and Planetary Evolution IV. Geological Society of America Special Paper 465, Boulder, Colorado, pp. 619–643.

Mohr-Westheide, T., Reimold, W.U., Riller, U., Gibson, R.L., 2009. Pseudotachylitic breccia and microfracture networks in Archean gneiss of the central uplift of the Vredefort impact structure, South Africa. South African Journal of Geology 112, 1–22.

Moser, D.E., 1997. Dating the shock wave and thermal imprint of the giant Vredefort impact, South Africa. Geology 25, 7–10.

Moser, D.E., Cupelli, C.L., Barker, I.R., Flowers, R.M., Bowman, J.R., Wooden, J., Hart, J.R., 2011. New zircon shock phenomena and their use for dating and reconstruction of large impact structures revealed by electron nanobeam (EBSD, CL, EDS) and isotopic U–Pb and (U–Th)/He analysis of the Vredefort dome. Canadian Journal of Earth Sciences 48, 117–139.

Ni, Y., Hughes, J.M., Mariano, A.N., 1995. Crystal chemistry of the monazite and xenotime structures. American Mineralogy 80, 21–26.

Ohno, I., Harada, K., Yoshitomi, C., 2006. Temperature variation of elastic constants of quartz across the α-β transition. Physics and Chemistry of Minerals 33, 1–9.

Potter, R.W.K., Kring, D.A., Collins, G.S., Kiefer, W.S., McGovern, P.J., 2013. Numerical modeling of the formation and structure of the Orientale impact basin. Journal of Geophysical Research: Planets 118, 963–979.

Reimold, W.U., 1995. Pseudotachylite in impact structures – generation by friction melting and shock brecciation? A review and discussion. Earth-Science Reviews 39, 247–265.

Reimold, W.U., Gibson, R.L., 2005. "Pseudotachylites" in Large Impact Structures, in: Koeberl, C., Henkel, H., (Eds.), Impact tectonics. Springer, Berlin Heidelberg, pp. 1–53.

Reimold, W.U., Colliston, W.P., 1994. Pseudotachylites of the Vredefort Dome and the surrounding Witwatersrand Basin, South Africa, in: Dressler, B.O., Grieve, R.A.F., Sharpton, V.L. (Eds.), Large Meteorite Impacts and Planetary Evolution. Geological Society of America Special Paper 293, Boulder, Colorado, pp. 177–196.

Reimold, W.U., Leroux, H., Gibson, R.L., 2002. Shocked and thermally metamorphosed zircon from the Vredefort impact structure, South Africa: a transmission electron microscopic study. European Journal of Mineralogy 14, 859–868.

Reimold, W.U., Hoffmann, M., Hauser, N., Schmitt, R-T., Zaag, P.T., Mohr-Westerheide, T., 2016. A geochemical contribution to the discussion about the genesis of impact-related pseudotachylitic breccias: Studies of PTB in the Otavi and Kudu Quarries of the Vredefort Dome support the “In Situ Formation” hypothesis. South African Journal of Geology 119, 453–472.

Reimold, W.U., Hauser, N., Hansen, B.T., Thirlwall, M., Hoffmann, M., 2017. The impact pseudotachylitic breccia controversy: Insights from first isotope analysis of Vredefort impact-generated melt rocks. Geochimica et Cosmochimica Acta 214, 266–281.

Riller, U., Lieger, D., Gibson, R.L., Grieve, R.A.F., Stöffler, D., 2010. Origin of large-volume pseudotachylite in terrestrial impact structures. Geology 38, 619–622.

Riller, U., IODP–ICDP Expedition 364 Science Party, 2018. Rock fluidization during peak-ring formation of large impact structures. Nature 562, 511–518.

Ringdalen, E., 2014. Changes to quartz during heating and the possible effects on Si production. Journal of the Minerals, Metals & Materials Society 67, 484–492.

Schmieder, M., Kring, D.A., 2020. Earth's Impact Events Through Geologic Time: A List of Recommended Ages for Terrestrial Impact Structures and Deposits. Astrobiology 20, 91–141.

Schreyer, W., 1983. Metamorphism and Fluid Inclusions in the Basement of the Vredefort Dome, South Africa: Guidelines to the Origin of the Structure. Journal of Petrology 24, 26–47.

Spray, J.G., 2010. Frictional melting processes in planetary materials: From hypervelocity impact to earthquakes. Annual Review of Earth and Planetary Science 38, 221–254.

Spray, J.G., Kelley, S.P., Reimold, W.U., 1995. Laser-probe $^{40}Ar/^{39}Ar$ dating of coesite- and stishovite-bearing pseudotachylytes and the age of the Vredefort impact event. Meteoritics 30, 335–343.

Swamy, V., Saxena, S., 1994. A thermodynamic assessment of silica phase diagram. Journal of Geophysical Research 99, 11787–11794.

Thompson, L.M., Spray, J.G., 1996. Pseudotachylyte petrogenesis: constraints from the Sudbury impact structure. Contributions of Mineralogy and Petrology 125, 359–374.

Willemse, J., 1937. On the old granite of the Vredefort Region and some of its associated rocks. Transactions of the Geological Society of South Africa 40, 43–119.

Wilshire, H.G., 1971. Pseudotachylite from the Vredefort Ring, South Africa. The Journal of Geology 79, 195–206.

Youssof, M., Thybo, H., Artemieva, I.M., Levander, A., 2013. Moho depth and crustal composition in Southern Africa. Tectonophysics 609, 267–287.

Figure Captions

Figure 1. Sampling locality and photographs of the outcrops. A: Inlay of South Africa with the location of the Vredefort Dome, and simplified geological map of the Vredefort structure, modified after Buchanan and Reimold (2002). The sampling locality is marked with a white cross. B: Dolerite outcrop with PT vein network. A black arrow denotes rounded granite clasts. C: Dolerite outcrop with 2 types of veins: Melt 1 (dark-brown) contains dolerite clasts, Melt 2 (pink) contains multiple mm-size granite clasts, as well as dolerite clasts. D: Outcrop of the massive PT with granite clasts at the contact between granite (left, not seen in the photograph) and dolerite (right).

Figure 2. WD-XRF analyses results. A: Total alkali-silica classification of samples in this study (LeBas et al., 1986). B: Trace element concentrations in rocks of this study. Melt 1 is slightly more mafic than the host dolerite, whereas Melt 2 systematically shifts towards granitic composition. PTs from the contact zone and within the granite have a composition of the host granite.

Figure 3. PTs in dolerite. A: Photograph of a sample surface with PT veins and a large (~24 mm in length) rounded granitic clast. Arrow points to a lens of Melt 2 within the Melt 1. B: Schematic sketch of the sample surface shown in (A). Host dolerite is in grey, "Melt 1" is a lighter melt phase with no granitic clasts, "Melt 2" is a darker melt with a granitic clast coded by "+". Areas for (C) and (D) are indicated. C: Chemical map of combined Si, Sr, and Ba. The host dolerite contains PTs with Melt 1 (orange, right). The contact with Melt 2 is in light-blue, numerous clasts of granitic affinity are in light-blue (left). D: Chemical map of combined Si, K, Rb, and Sr. The large granite clast with smaller granitic fragments within the Melt 2 are visible (pink and light-blue, top left, bottom centre). The vein network hosts clasts of coarse-grained dolerite (gabbro) distinct from the finer-grained host dolerite, suggesting

that coarse-grained dolerite analogue composes another type of exotic clast. The Si-K-rich light-green lens separating Melt 1 and Melt 2 is visible (top right).

Figure 4. The petrological context for the analysed shocked minerals. A: Photograph of the thin section of dolerite with the PT vein (black) that contains granitic clasts (light). Area for (B) indicated by a rectangle. B: Backscattered electron image of a granitic clast within the melt vein in dolerite. Arrows indicate veinlets of melt, injecting into granite clast. Mineral abbreviations: *Ap* = apatite, *Bt* = biotite, *Kfs* = K-feldspar, *Mnz* = monazite, *Pl* = plagioclase, *Q* = quartz, *Zrn* = zircon.

Figure 5. EBSD data on shocked minerals. The petrological context is shown in Fig. 4. A: Cumulative misorientation EBSD map of zircon, arrows point to discontinuous twin lamella. B: Equal-area lower hemisphere projection pole figures, showing [001] and <110> axes of the host grain (blue to white) and microtwin lamellae (red to white). Black points are zircon domains, which are not color-coded. C: Cumulative misorientation EBSD map of monazite adjacent to zircon in (A). Arrows point to two sets of microtwin lamellae, color-coded green and red. D: Pole figures of [001], [010] and [100] axes of the host grain (blue to white) and microtwin lamellae (green and red).

Figure 6. Phase transition diagram for SiO_2, after Swamy and Saxena (1994). A hypothetical clockwise *P-T* path for quartz in granite is shown by a dashed blue line, and the path for quartz in pseudotachylite in granite is shown by a solid red line. The red and blue triangles represent the relative molar size of the SiO_2 phase with respect to α-quartz (black empty triangle); see also Figure 7. Molar volumes for SiO_2 phases are from Swamy and Saxena (1994). *P-T* conditions: starting conditions calculated as 100–150 MPa and 400ºC based on pre-impact depth of 10–15 km (Schreyer, 1983; Gibson et al., 1998), and post-shock temperatures from Ivanov (2005) and Ivanov and Deutsch (1999). Crs = cristobalite.

Figure 7. Histograms representing molar volumes of the discussed SiO_2 phases. These phase transitions would be experienced by SiO_2 in an impact event, with the pre-shock alpha quartz on the left, and subsequent phases in expected order of transition.

Figure 8. Optical plane-polarized images of recrystallized and partially molten quartz textures, preserved in the clasts in pseudotachylite veins in granite. In D and F resorption of clasts occurs along the semi-circular boundaries, which could potentially be remnants of ballen texture.

Figure 9. Schematic sketch summarizing the incorporation process of granitic clasts into dolerite-hosted PTs. *Stage 1:* the shock wave passes, shock wave forms initial PT at the contact and within granite and dolerite. Minerals are shocked at this stage. Post-shock reverberations cause fracturing of the dolerite while the temperature of the system increases (Kenkmann et al., 2000; Ivanov, 2005; Riller et al., 2018). *Stage 2:* SiO_2 transitions from α-quartz to β-quartz, tridymite and, locally, β-cristobalite, resulting in significant volume expansion, driving the further development of the PT zone between gabbro and granite, and initiating more fractures within dolerite. The opening of fractures creates a negative pressure gradient within the dolerite body. Granite fragments and melt are injected into the adjacent dolerite. *Stage 3:* Granitic clasts are transported through the dolerite-hosted PTs. As temperature decreases, SiO_2 transitions back to α-quartz and fractures in dolerite narrow, trapping the granite clasts inside.

Figure 1

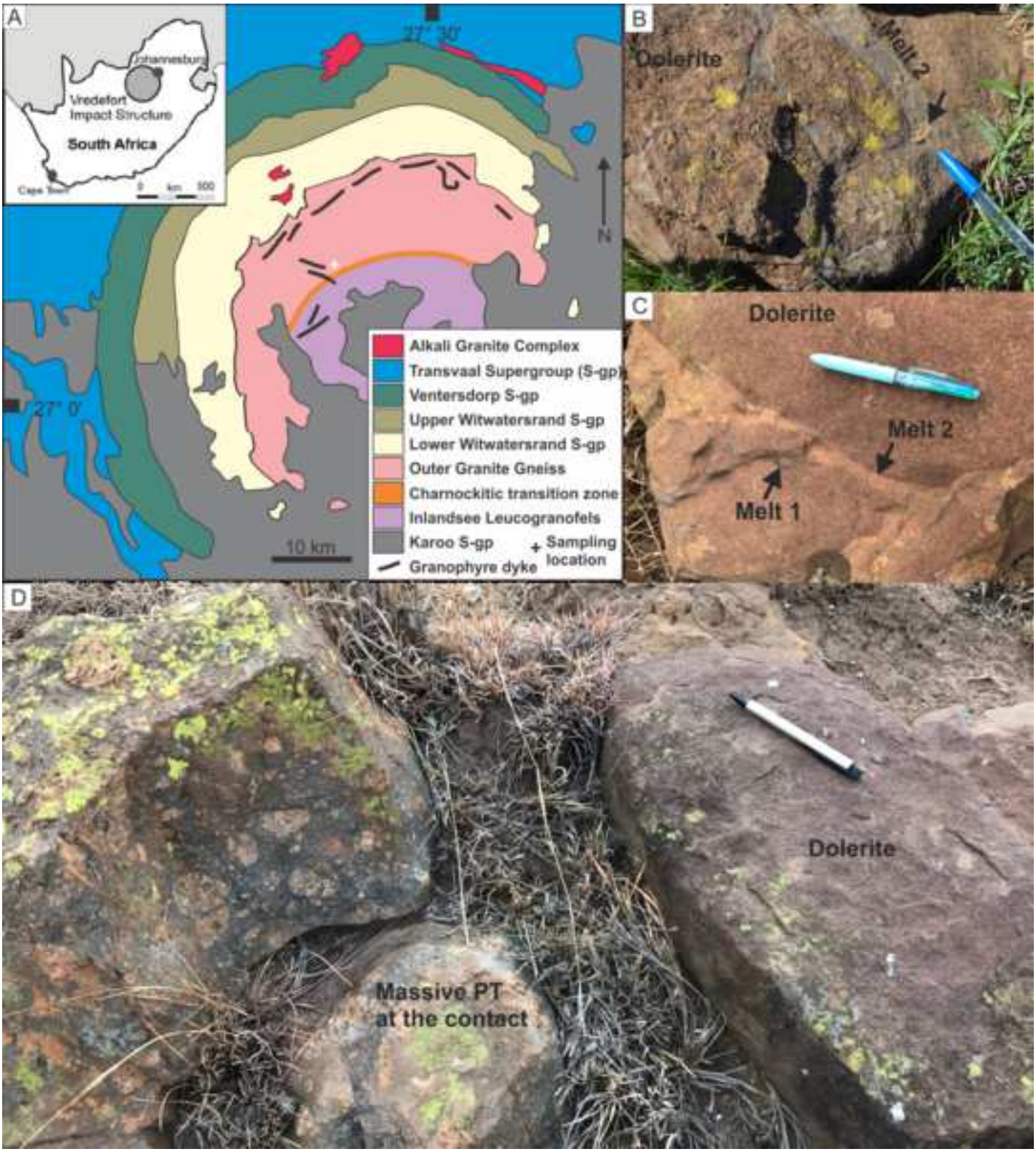
A
Johannesburg
Vredefort
Impact Structure
South Africa
Cape Town
0 km 500
27° 30'
27° 0'
N
10 km
Alkali Granite Complex
Transvaal Supergroup (S-gp)
Ventersdorp S-gp
Upper Witwatersrand S-gp
Lower Witwatersrand S-gp
Outer Granite Gneiss
Charnockitic transition zone
Inlandsee Leucogranofels
Karoo S-gp
Granophyre dyke
Sampling location
B
Dolerite
Melt 2
C
Dolerite
Melt 2
Melt 1
D
Dolerite
Massive PT
at the contact

Figure 2

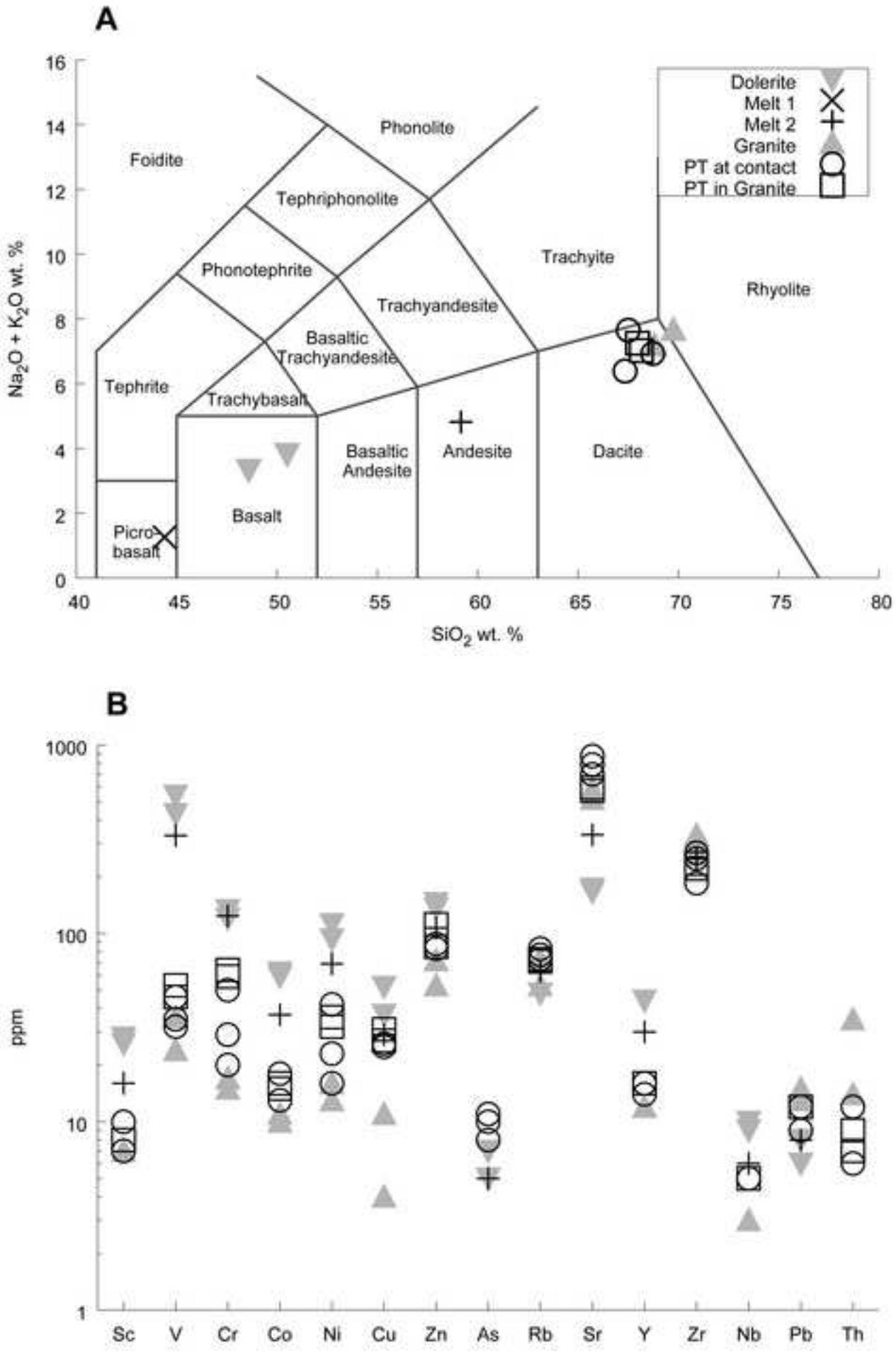
A
Dolerite
Melt 1
Melt 2
Granite
PT at contact
PT in Granite
Foidite
Phonolite
Tephriphonolite
Phonotephrite
Trachyandesite
Trachyite
Rhyolite
Basaltic Trachyandesite
Tephrite
Trachybasalt
Basaltic Andesite
Andesite
Dacite
Basalt
Picro basalt
$Na_2O + K_2O$ wt. %
SiO_2 wt. %
B
ppm
Sc
V
Cr
Co
Ni
Cu
Zn
As
Rb
Sr
Y
Zr
Nb
Pb
Th

Figure 3

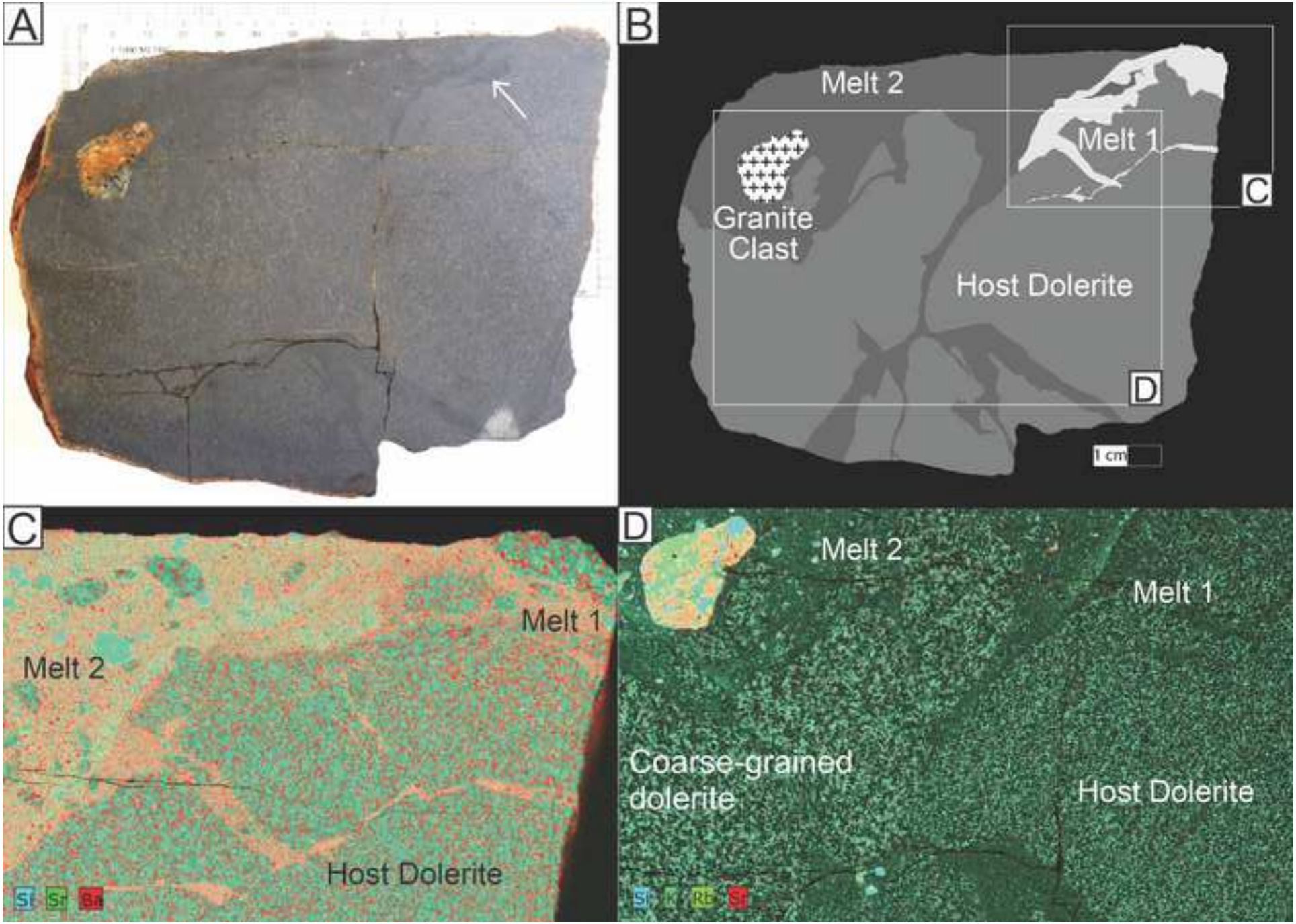
A
B
Melt 2
Melt 1
C
Granite
Clast
Host Dolerite
D
1 cm
C
Melt 1
Melt 2
Host Dolerite
Si
Sr
Ba
D
Melt 2
Melt 1
Coarse-grained
dolerite
Host Dolerite
Si
K
Rb
Sr

Figure 4

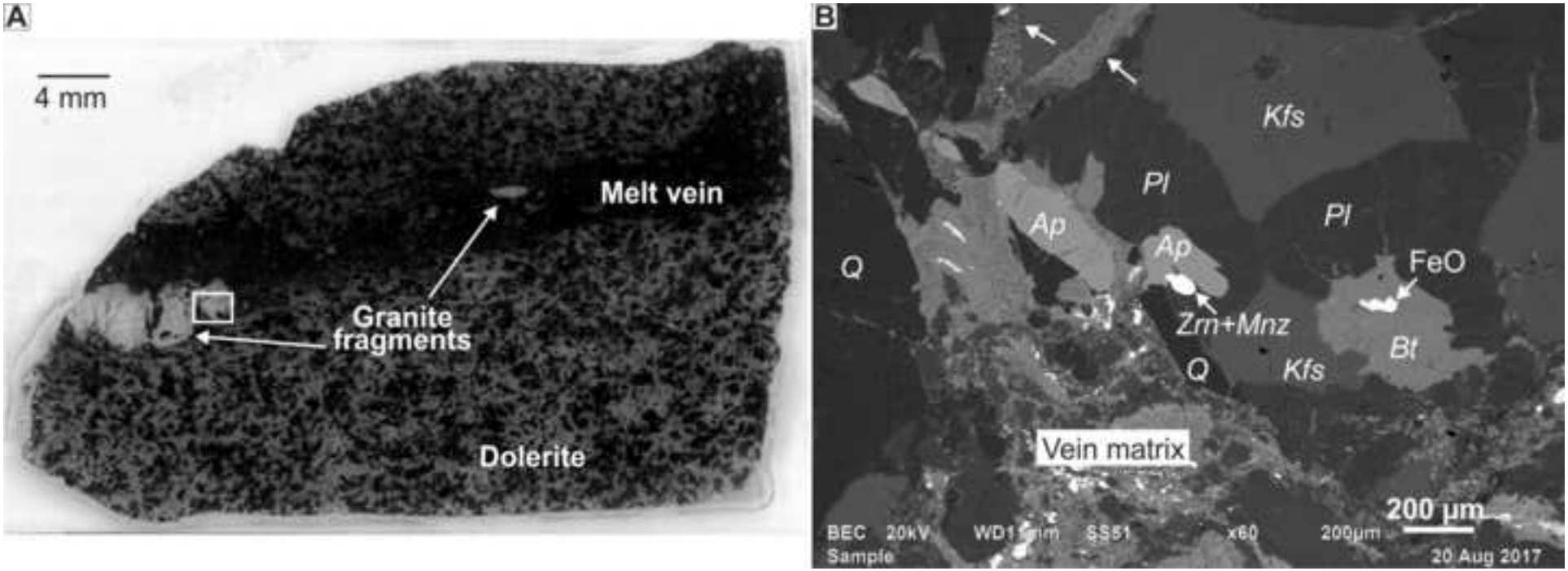
A
4 mm
Melt vein
Granite fragments
Dolerite
B
Kfs
Pl
Pl
Ap
Ap
Q
FeO
Zrn+Mnz
Bt
Q
Kfs
Vein matrix
200 µm
BEC 20kV WD1 mm SS51 x60 200µm
Sample
20 Aug 2017

Figure 5

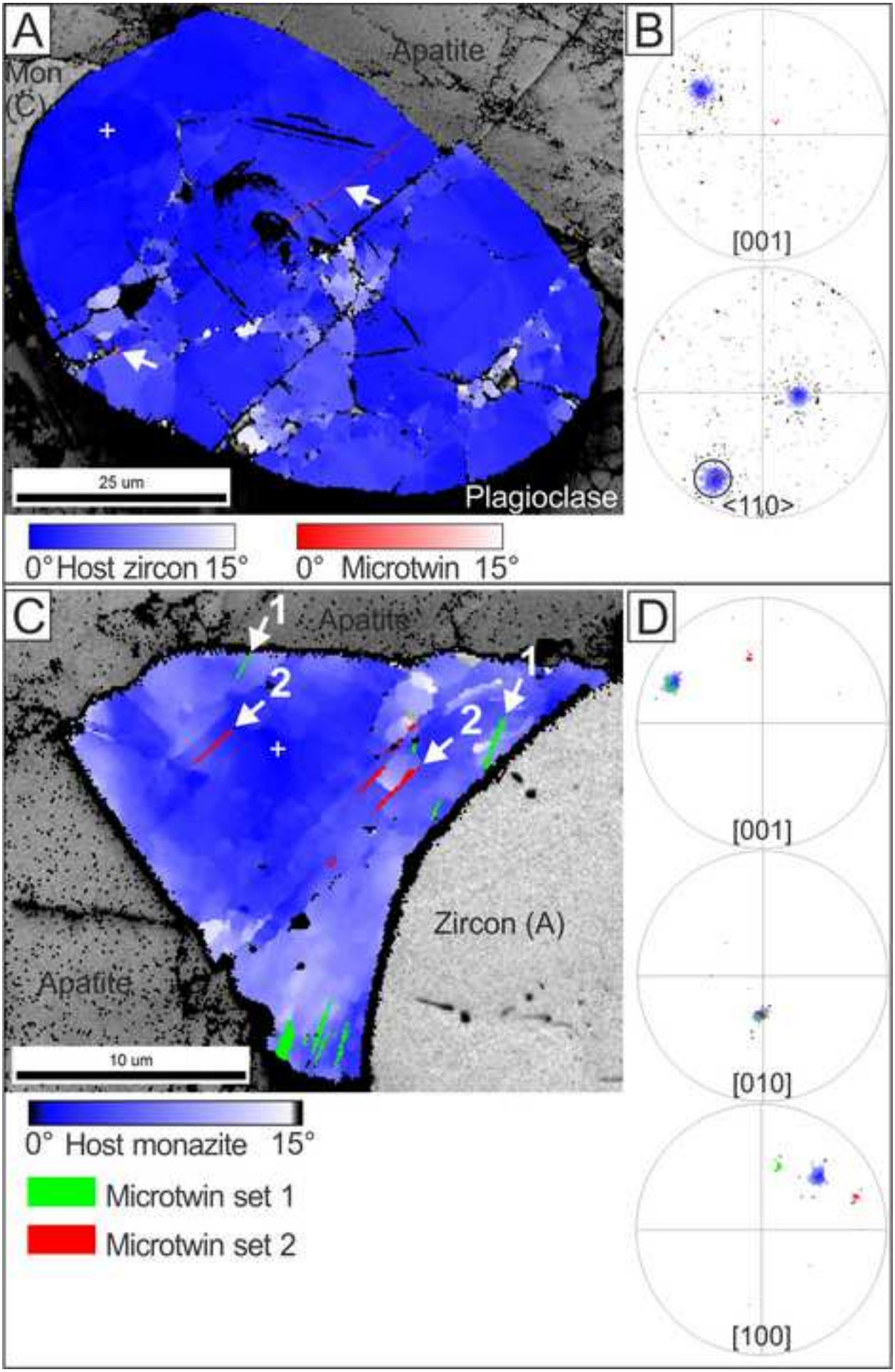
A
Mon
(C)
Apatite
25 um
Plagioclase
B
[001]
<110>
0° Host zircon 15°
0° Microtwin 15°
C
1
2
Apatite
Zircon (A)
Apatite
10 um
0° Host monazite 15°
Microtwin set 1
Microtwin set 2
D
[001]
[010]
[100]

Figure 6

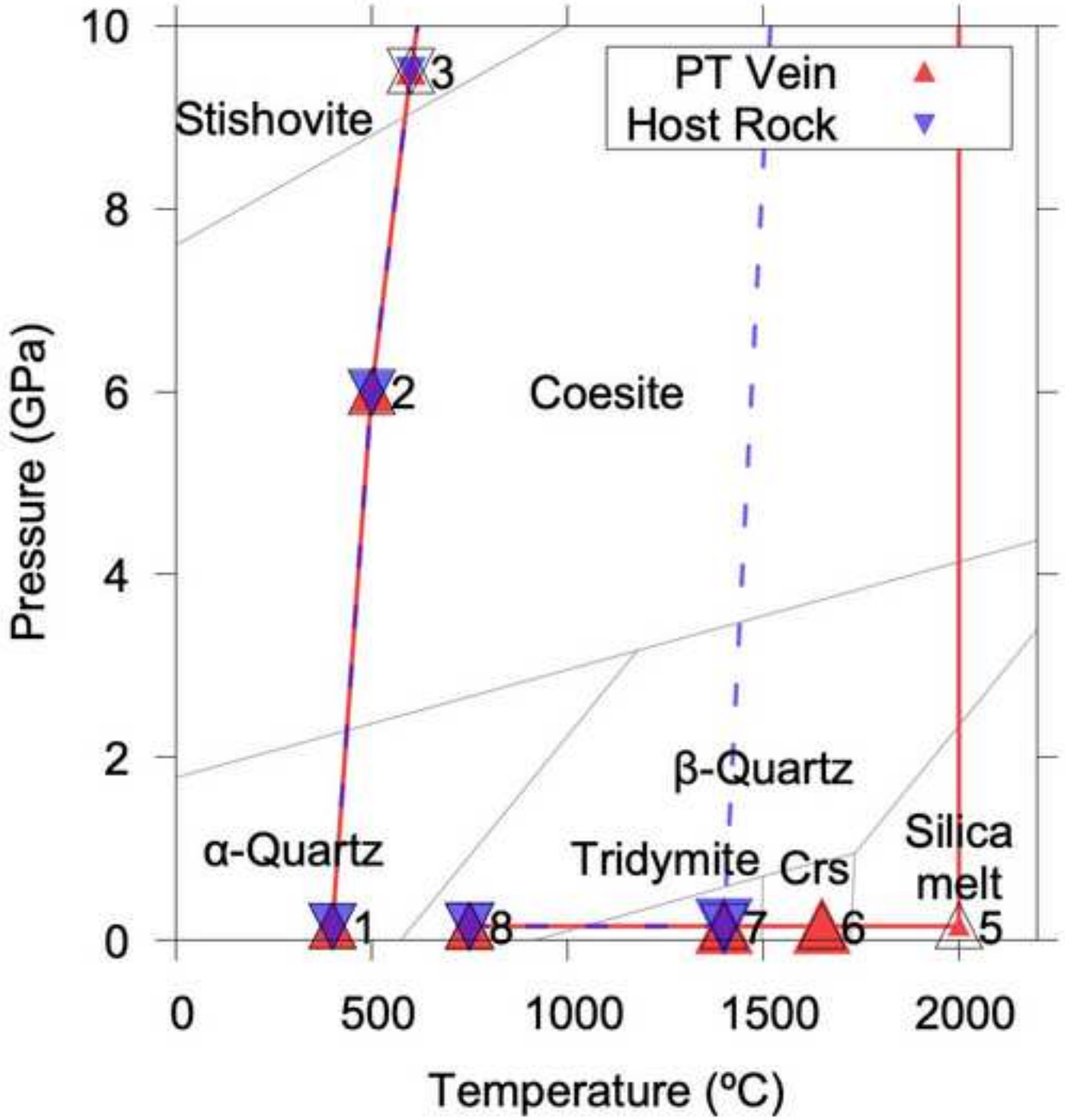
PT Vein
Host Rock
Stishovite
Coesite
α-Quartz
β-Quartz
Tridymite
Crs
Silica melt
1
2
3
5
6
7
8
Pressure (GPa)
Temperature (°C)
0
2
4
6
8
10
0
500
1000
1500
2000

Figure 7

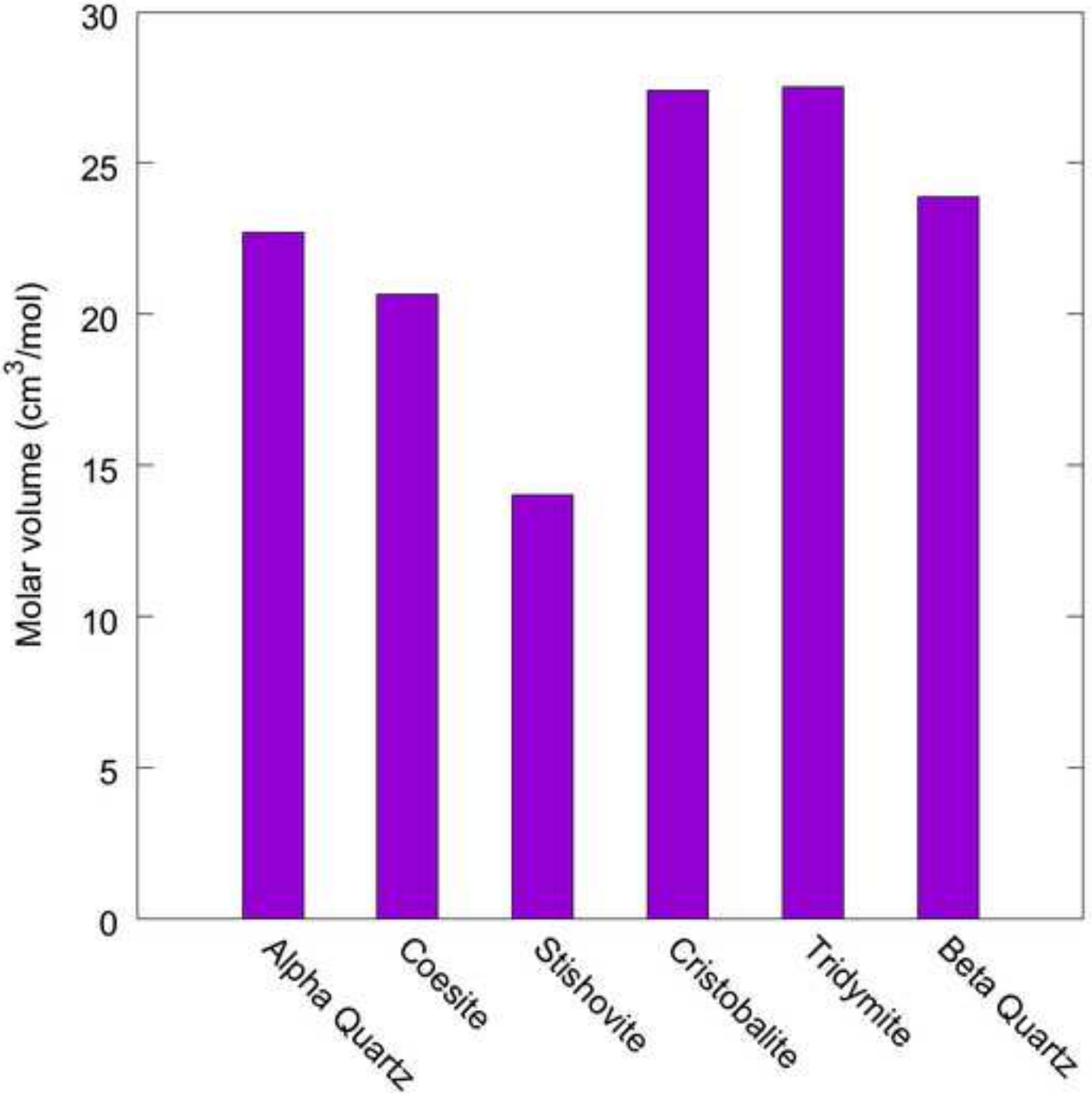
Molar volume (cm3/mol)
30
25
20
15
10
5
0
Alpha Quartz
Coesite
Stishovite
Cristobalite
Tridymite
Beta Quartz

Figure 8

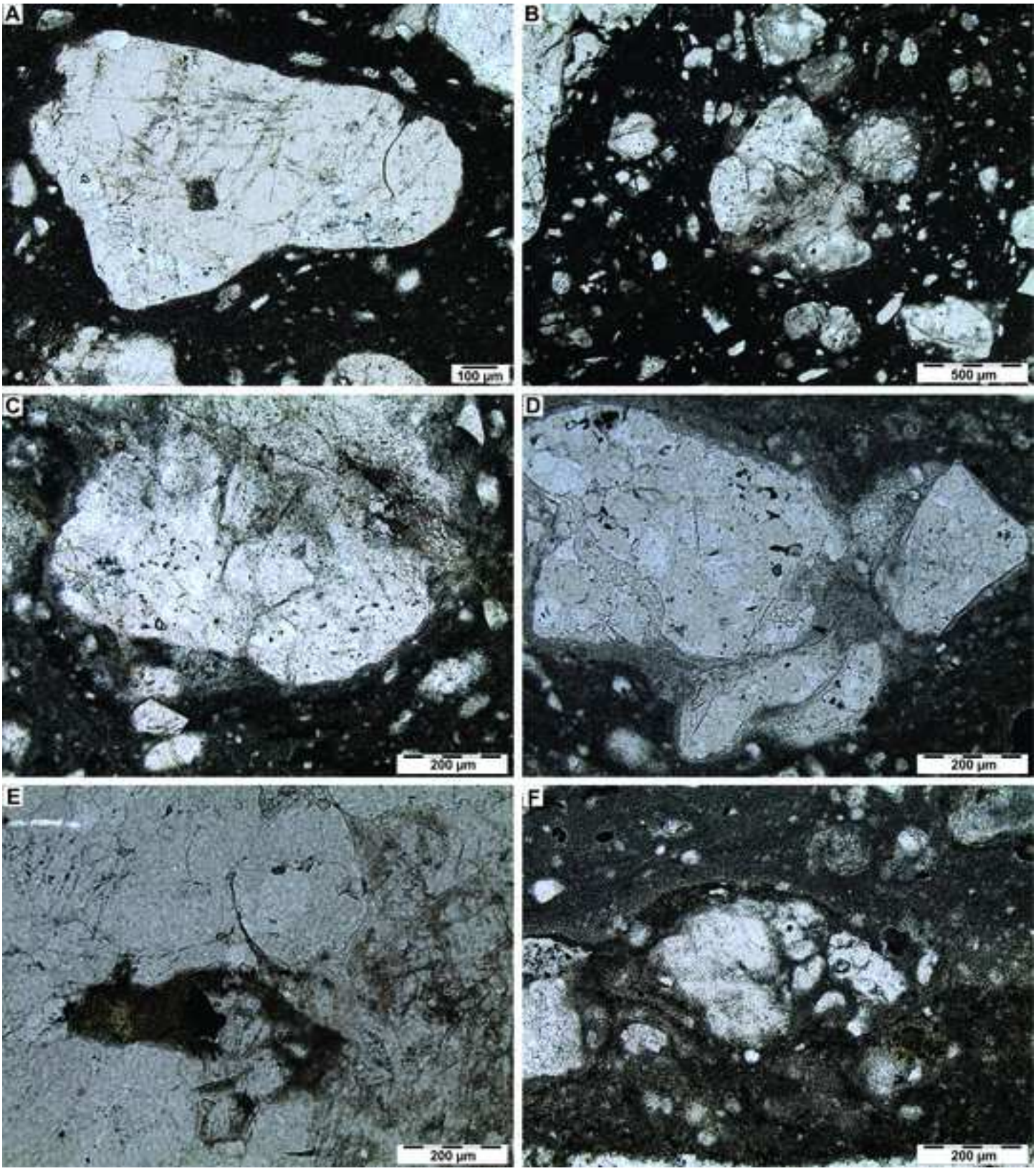

Figure 9

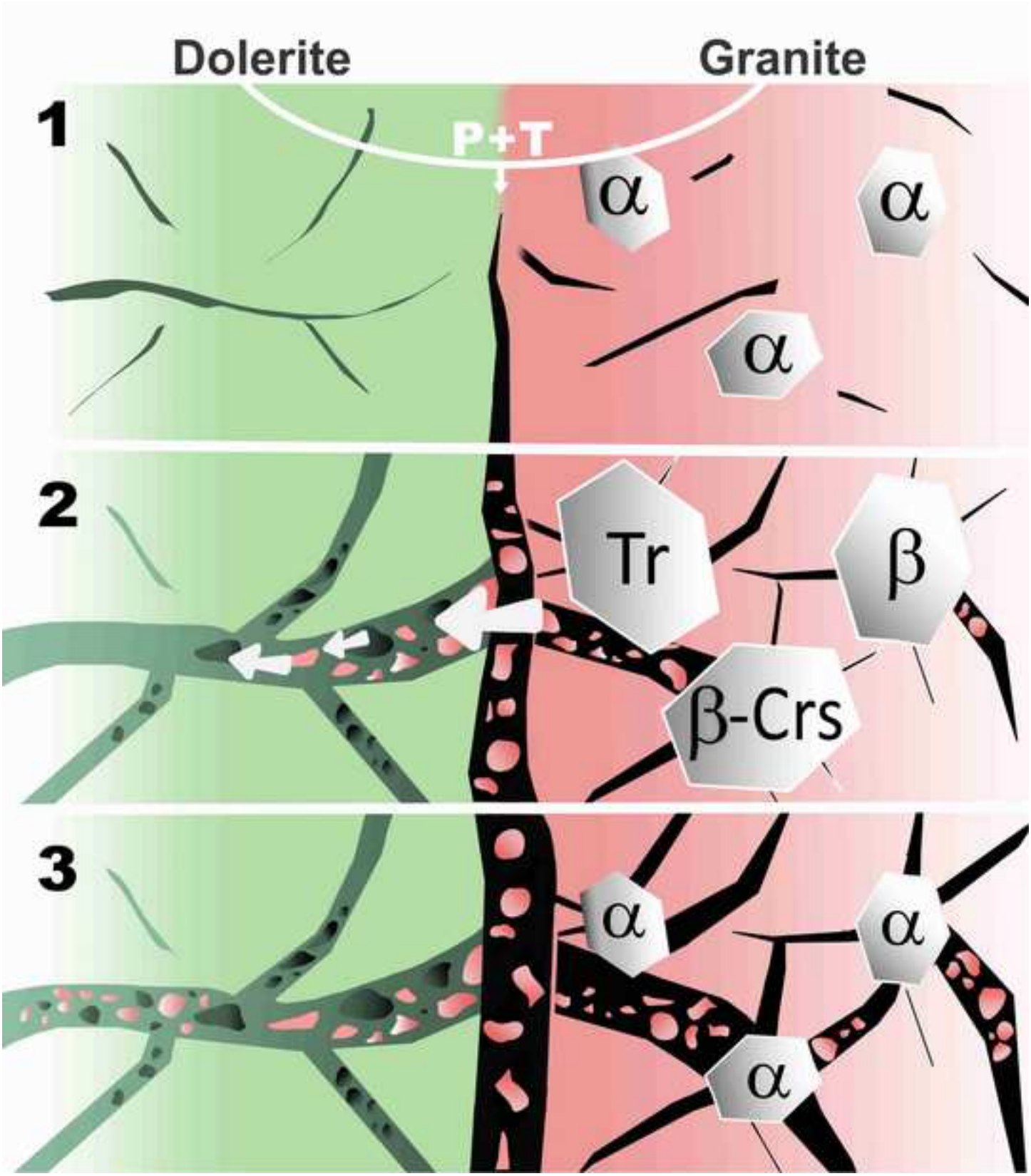

Rock	Dolerite	Melt 1 = vein in dolerite (no granite clasts)	Dolerite	Melt 2 = vein in dolerite with granite clasts	Massive PT at the contact zone			Granite		PT veins in granite	
Sample N	DGP16-09	DGP16-09-V	DGP16-11	DGP16-11B	CZD 18-01	CZD 18-02	CZD 18-03	GPT17-01 H1	GPT17-01 H2	GPT17-01 V1	GPT17-01 V2
SiO_2	48.59	44.4	50.51	59.17	68.73	67.51	67.35	68.81	69.76	68.16	67.97
TiO_2	2.51	2.36	2.43	1.51	0.49	0.5	0.56	0.4	0.35	0.46	0.52
Al_2O_3	12.08	11	11.43	12.61	15.34	15.58	15.14	14.98	15.61	13.99	15.19
Fe_2O_3	18.33	17.84	18.81	12.37	3.42	3.42	3.95	5.66	3.3	4.05	4.4
MgO	4.95	4.73	4.97	3.57	0.95	0.78	1.41	0.24	0.55	1.37	1.37
MnO	0.22	0.12	0.13	0.09	0.02	0.02	0.04	0.04	0.03	0.05	0.08
CaO	8.88	7.66	8.69	6.28	2.04	1.89	2.34	1.93	1.99	2.29	2.24
Na_2O	2.29	-	2.62	2.805	4.04	4.23	3.56	4.69	4.91	4.17	4.26
K_2O	1.04	1.26	1.2	2.01	2.89	3.42	2.83	2.5	2.76	2.85	2.99
P_2O_5	0.45	0.38	0.34	0.28	0.21	0.22	0.19	0.16	0.18	0.2	0.22
LOI	0.43	0.45	-0.26	0.71	0.68	0.7	1	0.6	0.26	0.64	0.73
Total	99.76	90.20	100.84	98.61	98.82	98.26	98.38	100.00	99.68	98.21	99.98

Table 1. WD-XRF analyses results (major elements), wt % oxides. LOI = loss on ignition, a measure of the weight loss when a sample is heated to 1050°C, expressed as wt%. The total of the DGP16-09-V is low, as the size of the analyzed sample was relatively small due to the difficulty of separation of the vein from the bulk sample. For the same reason, Na was not analyzed for this sample, as well as trace elements (see Table 2).

Rock	Dolerite			Melt 2 = vein in dolerite with granite clasts	Massive PT at the contact zone			Granite		PT veins in granite	
Sample N	DGP16-09	DGP-16-09 (re-analysed)	DGP16-11	DGP16-11-V	CZD 18-01	CZD 18-02	CZD 18-03	GPT16-01 H1	GPT16-01 H2	GPT16-01 V1	GPT16-01 V2
Sc	26	25	28	16	7	7	10	7	<7	<7	8
V	431	257	539	331	35	32	46	36	24	46	53
Cr	133	118	120	124	29	20	50	15	17	59	64
Co	62	50	59	37	13	13	18	11	10	15	16
Ni	112	81	93	69	23	16	42	16	13	32	36
Cu	52	83	37	29	25	25	26	11	4	31	27
Zn	145	147	136	107	83	83	88	72	53	85	112
As	7	n.d.	5	5	11	10	8	n.d.	n.d.	n.d.	n.d.
Rb	48	28	48	63	77	83	73	53	73	71	73
Sr	173	115	166	334	789	875	700	519	588	572	594
Y	44	32	44	30	14	14	16	12	12	16	16
Zr	255	156	256	250	250	268	185	334	259	221	235
Nb	10	9	9	6	5	5	5	3	3	5	5
Pb	6	4	8	8	12	12	9	15	13	12	12
Th	n.d.	4	n.d.	n.d.	6	12	6	35	14	7	9
U	n.d.	3	n.d.	n.d.	4	5	3	<2	2	2	3

Table 2. WD-XRF analyses results (trace elements), ppm, n.d. = not detected.